

Letter

# Geolocation Accuracy Assessment of Himawari-8/AHI Imagery for Application to Terrestrial Monitoring

Yuhei Yamamoto \*, Kazuhito Ichii, Atsushi Higuchi and Hideaki Takenaka

Center for Environmental Remote Sensing (CEReS), Chiba University, 1-33 Yayoi-cho, Inage-ku, Chiba 263-8522, Japan; ichii@chiba-u.jp (K.I.); higu@faculty.chiba-u.jp (A.H.); takenaka@ceres.cr.chiba-u.ac.jp (H.T.)

\* Correspondence: yamamoto\_y@chiba-u.jp

Received: 23 March 2020; Accepted: 24 April 2020; Published: 26 April 2020

**Abstract:** Recent advancements in new generation geostationary satellites have facilitated the application of their datasets to terrestrial monitoring. In this application, geolocation accuracy is an essential issue because land surfaces are generally heterogeneous. In the case of the Advanced Himawari Imager (AHI) onboard Himawari-8, geometric correction of the Himawari Standard Data provided by the Japan Meteorological Agency (JMA data) was conducted using thermal infrared band with 2km spatial resolution. Based on JMA data, the Center for Environmental Remote Sensing (CEReS) at Chiba University applied a further geometric correction using a visible band with 500m spatial resolution and released a dataset (CEReS data). JMA data target more general users mainly for meteorological observations, whereas CEReS data aim at terrestrial monitoring for more precise geolocation accuracy. The objectives of this study are to clarify the temporal and spatial variations of geolocation errors in these two datasets and assess their stability for unexpected large misalignment. In this study, the temporal tendencies of the relative geolocation difference between the two datasets were analyzed, and temporal fluctuations of band 3 reflectances of JMA data and CEReS data at certain fixed sites were investigated. A change in the geolocation trend and occasional shifts greater than 2 pixels were found in JMA data. With improved image navigation performance, the geolocation difference was decreased in CEReS data, suggesting the high temporal stability of CEReS data. Overall, JMA data showed an accuracy of less than 2 pixels with the spatial resolution of band 3. When large geolocation differences were observed, anomalies were also detected in the reflectance of JMA data. Nevertheless, CEReS data successfully corrected the anomalous errors and achieved higher geolocation accuracy in general. As CEReS data are processed during the daytime due to the availability of visible bands, we suggest the use of CEReS data for effective terrestrial monitoring during the daytime.

**Keywords:** Himawari-8; Advanced Himawari Imager; terrestrial monitoring; geolocation

---

## 1. Introduction

Himawari-8 is one of Japan's new geostationary satellites that has been operated by the Japan Meteorological Agency (JMA) since July 2015. The Advanced Himawari Imager (AHI) onboard Himawari-8 is superior to conventional imagers, as it has more visible and near-infrared wavelength bands [1], thereby enabling higher-dimensional terrestrial environment monitoring. For example, combination red band (AHI band 3: centered at 0.64  $\mu\text{m}$ ) and near-infrared band (AHI band 4: centered at 0.86  $\mu\text{m}$ ) reflectances provide indices for vegetation monitoring, such as normalized difference vegetation index (NDVI) and enhanced vegetation index 2 (EVI2) [2]. These indices have

been calculated globally using polar-orbiting satellite sensors such as Visible Infrared Imaging Radiometer Suite (VIIRS), and AHI can calculate them with high frequency. Miura et al. [3] calculated the NDVI over Japan, which has a temperate and humid climate, at a frequency of 10 min throughout a year. They showed that the high-temporal NDVI signature of AHI is useful for detecting spring green-up and fall brown-down periods, by comparing it with the temporal NDVI profile obtained from one of the latest polar-orbiting satellite sensors, VIIRS, onboard the Suomi-National Polar-orbiting Partnership (S-NPP). Furthermore, the combination of red band (AHI band 3) and shortwave infrared band (AHI band 5: centered at 1.6  $\mu\text{m}$ ) reflectances can be used to calculate an index to detect snow/ice coverage [4,5]. Such detection is effective for improving the accuracy of cloud detection and vegetation phenology analysis. In addition, the use of multiple visible, near-infrared and infrared bands has enabled the estimations of land surface physical quantities, such as leaf area index [6], land surface temperature [7], and incoming surface solar radiation [8].

The spatiotemporal resolution of AHI has also been improved, with about 0.5 km for band 3, about 1 km for bands 1, 2, and 4 (0.47, 0.51, and 0.86  $\mu\text{m}$ , respectively), and about 2 km for other infrared bands at the sub-satellite point. These spatial resolutions are twice those of the conventional sensor, Japanese Advanced Meteorological Imager (JAMI), onboard Multifunction Transport Satellite-2 (MTSAT-2). The observation cycle of the full disk is 10 min, which is six times higher than that of JAMI. These improvements of AHI enable the observation of the features of smaller-scale phenomena, such as urban heat islands [9,10] and biomass burning [11]. Its application is expected to be further extended to more fields, such as agriculture [12,13].

Despite the advantages, Himawari-8/AHI has a limitation in terms of geolocation accuracy in terrestrial monitoring. The Himawari standard data provided by JMA (JMA data) are geometrically corrected by a phase-only-correlation (POC) method [14,15] using two infrared bands [16]. These bands cover land surface features during both day and night, but their spatial resolutions are coarser than those of the visible bands. Terrestrial monitoring using the visible/near-infrared bands and studies focusing on small-scale phenomena such as urban or agricultural areas require a geolocation accuracy higher than that of JMA data (approximately 2 km). In addition, the magnitude and direction of geometric correction applied to JMA data are the same for full disks, but the original magnitude and direction are different for each west–east scan [17].

The Center for Environmental Remote Sensing (CEReS) at Chiba University distributes full-disk AHI data (CEReS data) that have been geometrically corrected and resampled to latitude/longitude coordinates. The geolocation is performed by a POC method, similar to the method applied to JMA data, but using AHI band 3 data [18]. This geometric correction is limited only to daytime when band 3 reflectance data can be used, but it provides a higher spatial resolution (approximately 500 m). Furthermore, it is expected that the high spatial resolution facilitates the capturing of more clear-sky pixels, thereby suppressing failures due to local solutions in the POC procedure. The geometric correction of JMA and CEReS regard geolocation errors as components of two orthogonal axes over a plane of landmark chips, although errors related to attitude control should be expressed by angles of three axes (roll, pitch, and yaw).

The long-term variation in Himawari-8 geolocation errors has not been evaluated. Matsuoka et al. [19] used Terra/MODIS surface reflectance product (MOD09Q1) [20] as reference data and performed geometric correction by a cross-correlation (XC) method using AHI band 3 images. Similar to the POC method, the XC method uses satellite images and a reference map such as terrain data for pattern matching [21,22]. Their analysis showed that the geolocation error of JMA data had diurnal change in the scan (west–east) direction and its diurnal range reached 4 pixels for band 3. They also reported that geolocation errors in scan and cross-scan directions differed substantially from scan to scan. However, they focused on only a rapid scan imagery around Japan, and the analysis dates were two days, May 2, 2015 in the test operation period and July 31, 2015 in the operation period. Tan et al. [23] evaluated the long-term geolocation accuracy of the Advanced Baseline Imager (ABI) aboard the United States' Geostationary Operational Environmental Satellite 16 and 17 (GOES-16 and GOES-17) from the start of their postlaunch test up to 2019. The analysis showed that the accuracy was within 15 and 28  $\mu\text{rads}$ , the latter corresponding to 2 pixels of AHI band 3, and thereby achieved

quality requirements. They reported that the gradual increase in error over the long term was due to a fault in the spacecraft's Earth orientation calculations and a tendency towards greater errors in the west–east direction than in the north–south direction. The geolocation accuracy of the Geostationary Ocean Color Imager (GOCI) onboard the South Korean Communication, Ocean, and Meteorological Satellite (COMS) was evaluated from 2011 to 2017, focusing on targets in Northeast Asia [24]. The results showed that geometric correction for the GOCI has an accuracy within 1 pixel of GOCI (28  $\mu$ rad). Wolfe and Nishihama [25] reported that the long-term trend of geolocation errors of Terra/Aqua MODIS included a yearly cyclic term in both track and scan directions. AHI may also have some temporal change tendencies of the geolocation error in full-disk observations from the start of the operation to the present. The tendencies have to be clarified in order to ensure high-quality discussions in terrestrial remote sensing.

In this study, we investigated the geolocation difference during the daytime between JMA data and CEReS data. This analysis aims to show the temporal tendencies of the relative geolocation difference between the two datasets, and to clarify the causes of those tendencies. In addition, focusing on a case with a large number of geolocation differences, we investigated the temporal fluctuations of band 3 reflectances of JMA data and CEReS data at certain fixed sites caused by errors in geolocations, as described in Sections 2.3.2 and 3.2. In this manner, the stability of both datasets in terrestrial monitoring was evaluated.

## 2. Materials and Methods

### 2.1. Geographic Range

The study area is located at 85°E–205°E (155°W), 60°N–60°S, defined in the Himawari-8 AHI data provided by CEReS (Figure 1). The target area covers very wide geographic regions, ranging from Northern Asia to Oceania, including tropical Asia and very wide temperature and precipitation gradients from tropical to boreal climate and from humid tropical and temperate regions to semiarid and arid regions.

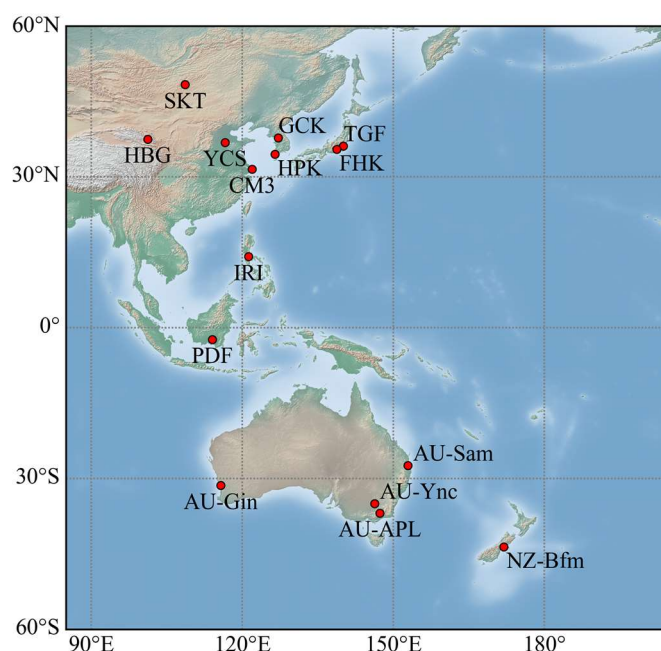


**Figure 1.** Spatial distribution of the selected site. Detailed information on site abbreviations is shown in Table 1. The geographic range of this figure is based on the spatial coverage of Himawari-8 AHI dataset provided by the Center for Environmental Remote Sensing (CEReS), Chiba University.

### 2.2. Himawari-8 AHI datasets

We used two different Himawari-8 AHI datasets in this study to evaluate their geolocation accuracies. The first one is JMA data provided as an original Himawari-8 AHI dataset by JMA, Japan. The dataset is commonly used in various applications [26–31]. The other one is CEReS data provided by CEReS, Chiba University [32]. The CEReS data are generated by applying further geometric corrections (V20151105) to JMA data aiming at potential application to land surface observations, which require high geolocation accuracy [3,9,10,18].

The geometric correction of JMA data is conducted with a POC method [14,15], known as a pattern matching between a referential map and satellite images, using AHI bands 7 and 13 (centered at 3.9  $\mu\text{m}$  and 10.4  $\mu\text{m}$ , respectively) with a spatial resolution of approximately 2 km [16]. The geolocation calculation is performed every 10 min.

The CEReS data are geolocated by a POC method using AHI band 3 data [18]. As mentioned earlier, the CEReS data are resampled to the latitude/longitude coordinates after the geometric correction processing. Band 3 has a spatial resolution of 500 m at the sub-satellite point, and thus, CEReS band 3 data have a gridded resolution of 0.005°. Similarly, other data with spatial resolutions of 1 km (visible/near infrared) and 2 km (infrared) at the sub-satellite point are resampled to 0.01° and 0.02°, respectively. As with JMA data, the geolocation calculation is performed every 10 min.

We used column/line offset factors (COFF/LOFF), which are obtained after geometric correction, to compare the geolocations between CEReS data and JMA data (see Section 2.3.1), and the band 3 reflectance to evaluate the stabilities in fixed-site monitoring (see Section 2.3.2). The COFF and LOFF stand for offset factors in the column (west–east) and line (north–south) directions, respectively. As described above, uniform COFF/LOFF values are assigned to JMA data (i.e.,  $\text{COFF}_{\text{JMA}} = \text{LOFF}_{\text{JMA}} = 11000.5$ ), whereas different COFF/LOFF values are assigned to each scan of CEReS data. Thus, the numbers of COFF/LOFF in CEReS data are 22,000 for both according to the number of pixels of band 3 in the north–south direction (i.e.,  $\text{COFF}_{\text{CEReS}_i}$  and  $\text{LOFF}_{\text{CEReS}_i}$  ( $i = 1, 2, \dots, 22,000$ )). The COFF/LOFF differences between the two datasets indicate the difference in geolocation for each scan. If the geolocation of scan  $i$  in the JMA data is shifted eastward with the geometric correction of CEReS,  $\text{COFF}_{\text{CEReS}_i}$  becomes larger than  $\text{COFF}_{\text{JMA}}$ . Similarly, if the geolocation of scan  $i$  is shifted southward with the geometric correction of CEReS,  $\text{LOFF}_{\text{CEReS}_i}$  becomes larger than  $\text{LOFF}_{\text{JMA}}$ . Therefore, the positive value of a COFF difference at scan  $i$  ( $d\text{COFF}_i = \text{COFF}_{\text{CEReS}_i} - \text{COFF}_{\text{JMA}}$ ) indicates that the geolocation of CEReS data at scan  $i$  is east of JMA data (i.e., an eastward shift of the coastal geolocation seen in Figure 2a). The positive value of a LOFF difference at scan  $i$  ( $d\text{LOFF}_i = \text{LOFF}_{\text{CEReS}_i} - \text{LOFF}_{\text{JMA}}$ ) indicates that the geolocation of CEReS data at scan  $i$  is south of JMA data (i.e., a southward shift of the coastal geolocation seen in Figure 2b).

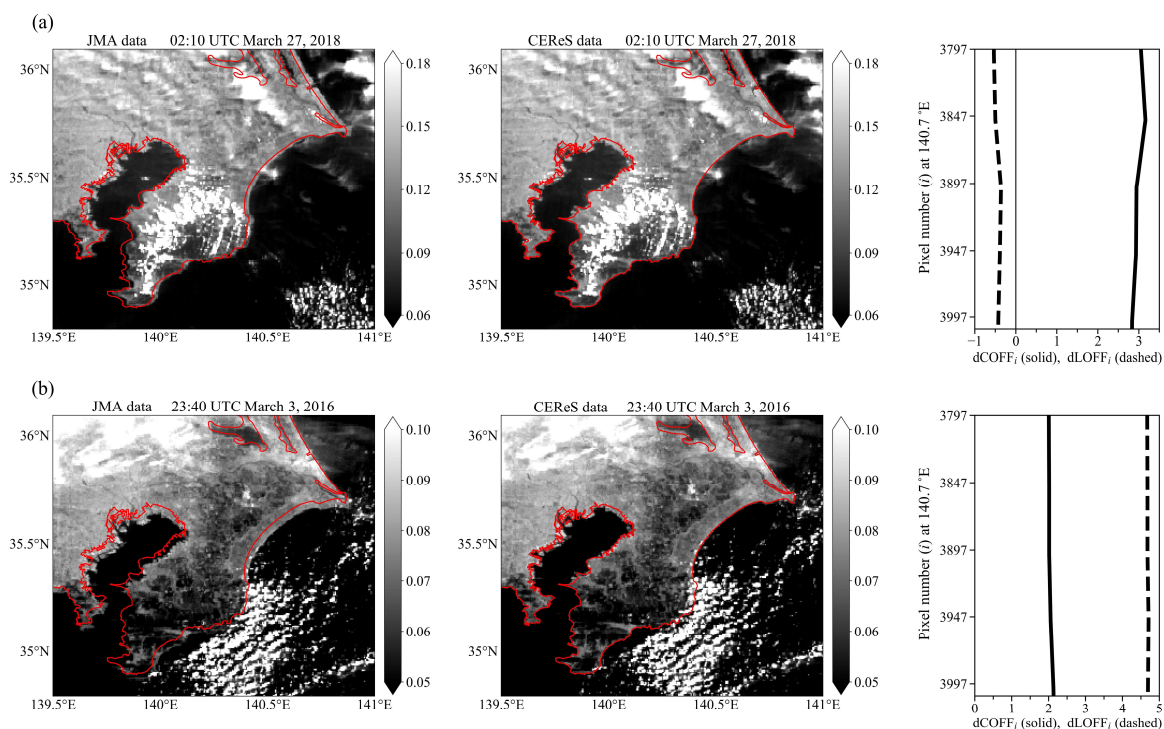


**Figure 2.** An example of band 3 reflectance images from Japan Meteorological Agency (JMA) data (left) and CERES data (center) for case (a) large positive  $dCOFF_i$  at 02:10 UTC on March 27, 2018 and case (b) large positive  $dLOFF_i$  at 23:40 UTC on March 3, 2016.  $dCOFF_i$  and  $dLOFF_i$  profiles corresponding to the scans ( $i = 3797, 3798, \dots, 4006$ ) (right) for the area shown in the left-hand images. The mean values of  $dCOFF$  and  $dLOFF$  for case (a) are 2.99 pixels and -0.43 pixels, respectively; for case (b) these are 2.04 pixels and 4.69 pixels, respectively.

### 2.3. Analysis

We conducted two analyses, relative geolocation evaluation (Section 2.3.1) and stability evaluation in fixed-site monitoring (Section 2.3.2). The former aims at identifying temporal tendencies of the relative geolocation difference between the two datasets and clarifying their geolocation characteristics through inter-comparison. The latter aims at exploring which datasets are more stable in terms of geolocation by comparing each dataset with reference at fixed sites.

The analysis period covered four years from July 7, 2015 to July 7, 2019, with a 10 min frequency for both analyses. For relative geolocation evaluation using  $dCOFF/dLOFF$ , we targeted a time period from 23:00 UTC to 07:00 UTC based on the ranges of daytime at the nadir of Himawari-8 and a selection of previous studies [3, 31]. For the stability evaluation using band 3 reflectance, we targeted the time from 8:00 to 16:00 local standard time of each selected site.

#### 2.3.1. Relative Geolocation Evaluation

We calculated the maximum, mean, and minimum values of  $dCOFF_i$  and  $dLOFF_i$  ( $i = 1, 2, \dots, 22000$ ) at each observation time, and investigated the tendencies of seasonal and annual changes of geolocation difference. In addition, we investigated diurnal changes of geolocation difference by averaging  $dCOFF$  and  $dLOFF$  at each observation time during the analysis periods. The frequency at which the geolocation difference becomes large for each scan and observation time was also analyzed.

#### 2.3.2 Stability Evaluation in Fixed-site Monitoring

We used the top-of-the-atmosphere band 3 reflectances of JMA data and CERES data. Regarding the sites considered in the analysis, we selected 15 sites from flux sites registered in AsiaFlux [33] and OzFlux [34], considering various environmental factors, such as inland/coastal and latitude zones

(see Table 1 and Figure 1). We focused on cases where the absolute value of dCOFF or dLOFF of the scan corresponding to each selected site was greater than 2 pixels.

The stability of geolocation accuracy was evaluated by comparing observation data (JMA data and CEReS data) and reference data (Figure 3). The observation data were created using reflectances of 3×3 pixels around a site using JMA data or CEReS data at time  $t$  when dCOFF or dLOFF was greater than 2 pixels. The reference data were created using reflectances of 3×3 pixels around a site at two periods: one scene before ( $t-10$  min), and one scene after ( $t+10$  min). When  $t$  was 02:30 UTC, the reflectances at  $t+20$  min were used instead of  $t+10$  min, because no image was produced due to routine satellite housekeeping at 02:40 UTC. Similarly, when  $t$  was 02:50 UTC, the reflectances at  $t-20$  min were used instead of  $t-10$  min. Fixed-site monitoring using remote sensing requires a clear-sky condition where observed reflectance is not affected by clouds, as a precondition. We applied a threshold-based cloud detection method based on Yamamoto et al. (2018) [7], to extract the cases in which 3×3 pixels around each site were under clear-sky in all three scenes (i.e.,  $t-10$ ,  $t$ , and  $t+10$  min). For the scenes of  $t-10$  min and  $t+10$  min, reflectances lower than the third quartile of the cases extracted by cloud detection were used for the analysis. This removal of outliers is to reduce the overlooking of cloud detection.

We averaged the reflectances at  $t-10$  min and  $t+10$  min of both JMA data and CEReS data and defined them as reference values of 9 pixels at  $t$ . The average value and standard deviation of the reflectances of the 9 pixels were regarded as spatial information of the pixels. We compared averages and standard deviation of the reflectances of JMA data ( $R_{obs\_JMA}$  and  $\sigma R_{obs\_JMA}$ , respectively) and CEReS data ( $R_{obs\_CEReS}$  and  $\sigma R_{obs\_CEReS}$ , respectively) with those of references ( $R_{ref}$  and  $\sigma R_{ref}$ , respectively). The data with the larger difference from  $R_{ref}$  and/or  $\sigma R_{ref}$  were judged as “misaligned”.

**Table 1.** List of selected sites used in this study. IGBP denotes the International Geosphere–Biosphere Programme, and IGBP land cover type is derived from the MODIS Land Cover Type (MCD12Q1) 500m product.

Flux site code	Latitude (°N)	Longitude (°E)	IGBP land cover
SKT	48.35	108.65	Deciduous needleleaf forest
GCK	37.75	127.16	Evergreen needleleaf forest
HBG	37.48	101.20	Grasslands
YCS	36.83	116.57	Croplands
TGF	36.11	140.10	Grasslands
FHK	35.44	138.76	Deciduous needleleaf forest
HPK	34.48	126.48	Croplands
CM3	31.52	121.96	Permanent Wetlands
IRI	14.14	121.27	Croplands
PDF	-2.35	114.04	Evergreen broadleaf forest
AU-Sam	-27.39	152.88	Woody Savannas
AU-Gin	-31.38	115.71	Woody Savannas
AU-Ync	-34.99	146.29	Grasslands
AU-APL	-36.86	147.32	Grasslands
NZ-Bfm	-43.59	171.93	Grasslands

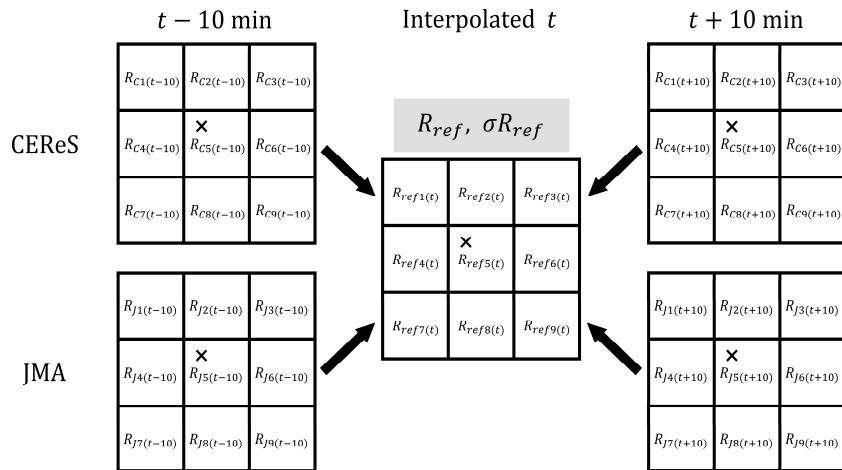


**Figure 3.** Schematic showing the calculation of reference pixel values at an observation time ( $t$ ). The average ( $R_{ref}$ ) and standard deviation ( $\sigma R_{ref}$ ) were calculated using interpolated  $3 \times 3$ -pixel values centered at the site (“X”); these were calculated using the mean of pixel values at  $t-10 \text{ min}$  and  $t+10 \text{ min}$  in both the CEReS and JMA data. These data were used for stability evaluation.

### 3. Results

#### 3.1. Relative Geolocation Evaluation

Based on the time-series of  $dCOFF_i$  and  $dLOFF_i$  ( $i = 1, 2, \dots, 22000$ ) shown in Figure 4, most shifts due to geometric correction by CEReS were within  $\pm 2$  pixels of band 3 spatial resolution (approximately  $\pm 1.0\text{--}1.4 \text{ km}$ ). Therefore, the geometric correction of JMA data was performed with a higher accuracy than the 2 km resolution of the infrared bands for the long term. Some cases, however, remarkably deviated from the range of  $\pm 2$  pixels (e.g., March 2018 in Figure 4a and September to December 2018 in Figure 4d), and the number and degree of the cases were both larger for  $dCOFF$  (Figure 4b vs Figure 4e and Figure 4c vs Figure 4f).

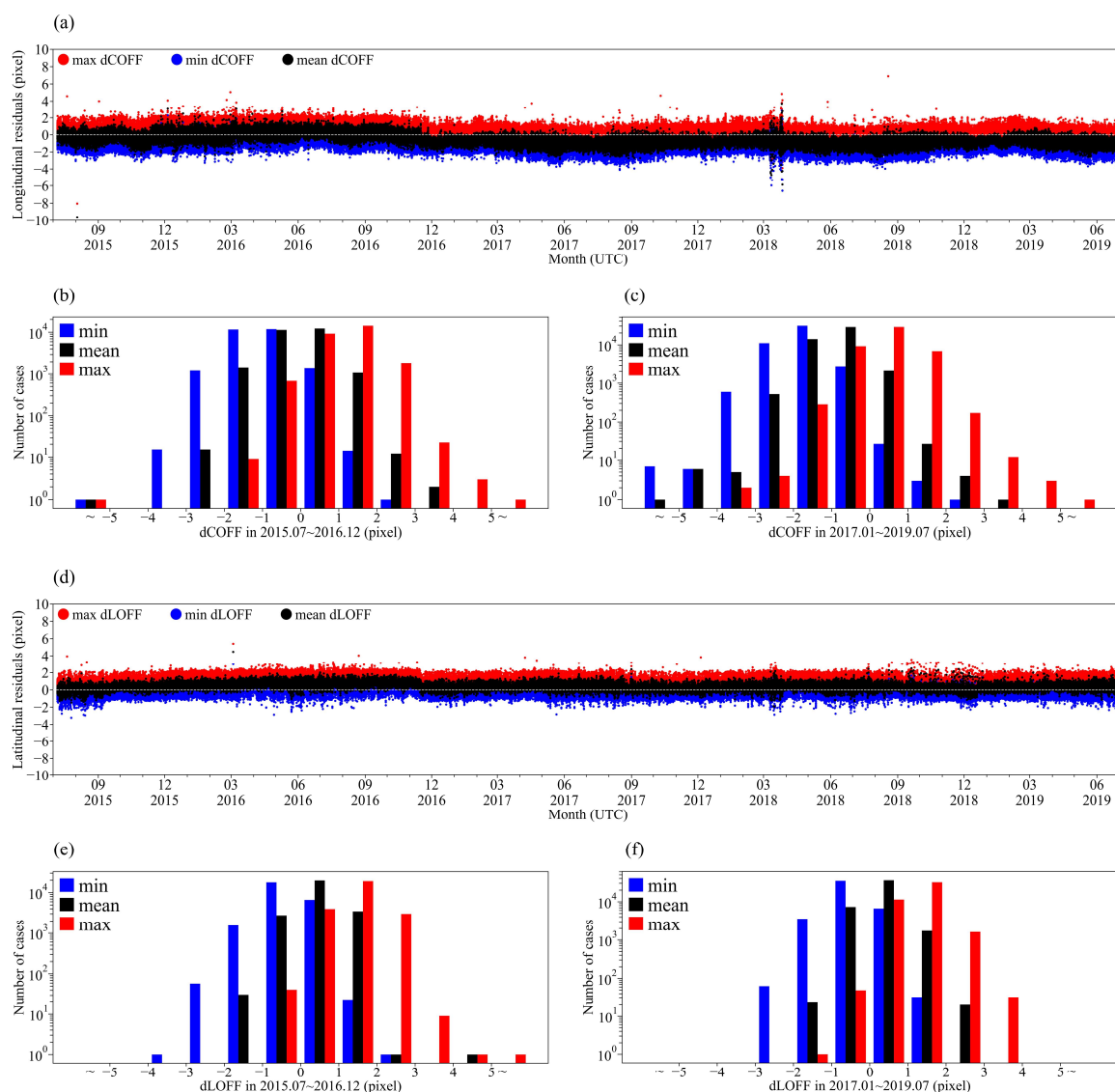


**Figure 4.** (a) Time series of the maximum, mean, and minimum values of COFF differences (dCOFF) for all 22,000 scans taken every 10 min as part of both JMA and CERES data. Histograms show the dCOFF for two periods: (b) July 2015 to December 2016 and (c) January 2017 to July 2019. Figure 4 (d), (e), and (f) show the same data as Figure 4 (a), (b) and (c), respectively, but for the dLOFF.

Both dCOFF and dLOFF showed shifts in the temporal trend after November–December 2016 (Figure 4a and Figure 4d). Mean dCOFF demonstrated a weak increasing trend from July 2015 to December 2016, while it became negative and showed seasonal fluctuation after December 2016. The number of cases of mean dCOFF smaller than  $-2$  pixels increased by about 500 cases after 2017 (Figure 4b vs Figure 4c). In terms of the seasonal fluctuation of dCOFF after December 2016, the mean dCOFFs approached zero and the range from the minimum to the maximum dCOFFs decreased from November–February, while the mean dCOFFs became substantially negative and the range from minimum to maximum increased from March–October. Regardless of this seasonal variation, large dCOFFs occurred frequently in March and April 2018. The mean dLOFF had a stronger increasing trend than the dCOFF from July 2015 to December 2016 and became steady, with slightly positive values after December 2016. It was rare for the dLOFF to deviate from  $\pm 2$  pixels and the number of the cases barely changed before and after 2017 (Figure 4e vs Figure 4f).

Different diurnal amplitudes were found between dCOFF and dLOFF and between two periods (Figure 5). As the long-term trends were shifted around December 2016 (Figure 4), we show the diurnal changes in two periods. For the period from July 2015 to December 2016, dCOFF was negative

in the morning and positive in the afternoon. On the other hand, dLOFF in the same period was positive in both the morning and afternoon, but slightly larger in the afternoon. From 2017, dCOFF decreased overall, while maintaining almost the same diurnal waveform of the previous period, and remained negative throughout the day. dLOFF in this period was slightly smaller than that of the previous period, while also maintaining almost the same diurnal waveform, and approached zero. In both dCOFF and dLOFF, the width of their 1 sigma range became smaller after 2017. In addition, both dCOFF and dLOFF tended to increase immediately after routine satellite housekeeping at 02:40 UTC, but they have been suppressed after 2017.

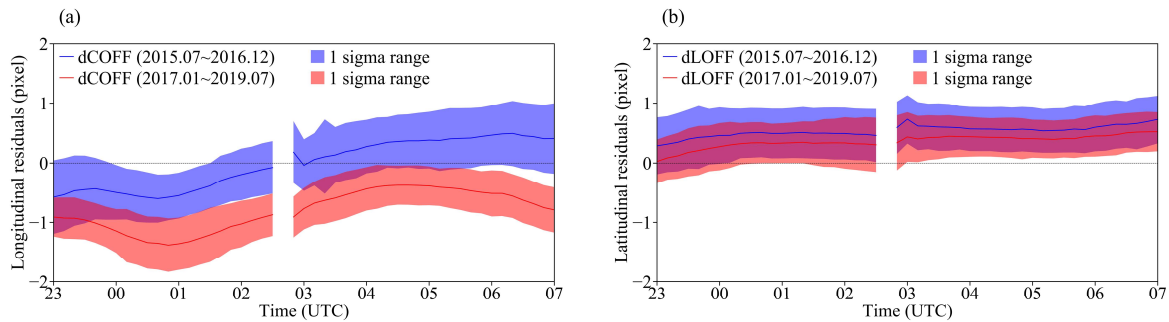


**Figure 5.** Diurnal changes of mean values and 1 sigma ranges of (a) dCOFF and (b) dLOFF at each observation time for two periods, from July 2015 to December 2016 (blue) and from January 2017 to July 2019 (red). The data at 02:40 UTC are missing due to routine satellite housekeeping.

Furthermore, large geolocation differences in the west–east direction between JMA data and CEReS data ( $dCOFF_i < 1$ ) occur differently depending on seasons and years (Figure 6). The occurrence ratio increased in the morning after 2017 (Figure 6 (a) vs (c) and (b) vs (d)), consistent with the tendency shown in Figure 5 (a). When the sun was north of the equator (from spring equinox to autumn equinox), the occurrence ratio in the morning was consistently high from north to south (Figure 6 (a) and (c)). On the other hand, when the sun was south of the equator (from autumn equinox to spring equinox), the ratio was high at low to middle latitudes in the Southern Hemisphere (pixel numbers around 11000 to 16000) (Figure 6 (b) and (d)). This seasonal variation was also observed in Figure 4.

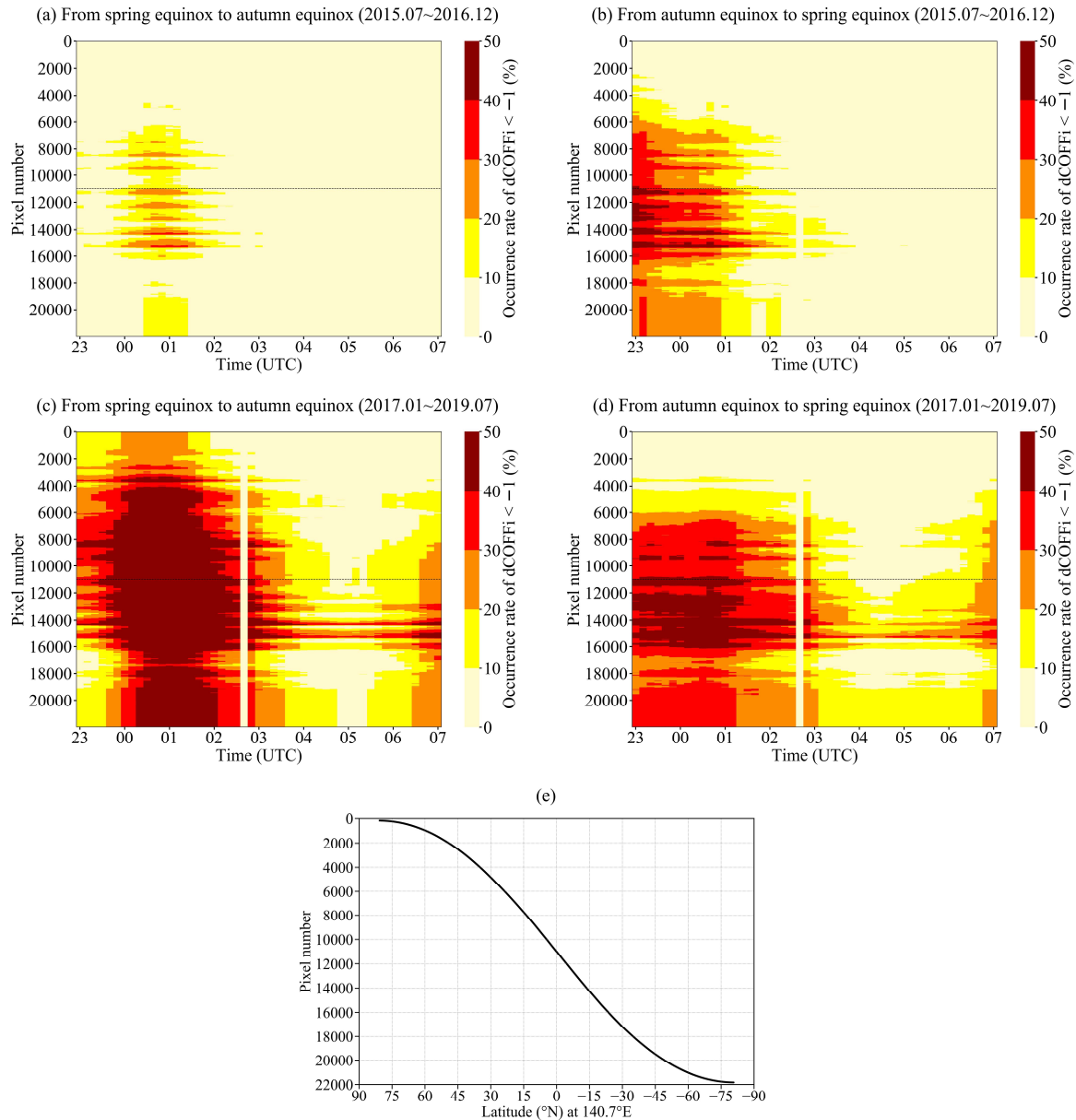


**Figure 6.** Occurrence ratios of cases with  $dCOFF_i$  less than  $-1$  pixel for each observation time and each scan. (a) The period from spring equinox to autumn equinox from July 2015 to December 2016. (b) The period from autumn equinox to spring equinox from July 2015 to December 2016. (c) and (d) The same as (a) and (b), respectively, but for the period from January 2017 to July 2019. Pixel numbers on the vertical axis represent the line numbers of the scan from north to south (from 1 to 22000). (e) The relationship between pixel number and latitude at  $140.7^\circ\text{E}$  where Himawari-8 flies.

### 3.2. Stability Evaluation in Fixed-site Monitoring

The cases extracted as anomalous pixels were distributed mainly from March to October after 2017 (Figure 7 for three sites (GCK, PDF, and NZ-Bfm) and Supplementary Materials for other twelve sites). These temporal distributions were consistent with larger  $dCOFF$  during this period, as shown in Figure 4a.

In most cases at many sites, the average and standard deviation of reflectances of CEReS data ( $R_{obs\_CEReS}$  and  $\sigma R_{obs\_CEReS}$ ) and JMA data ( $R_{obs\_JMA}$  and  $\sigma R_{obs\_JMA}$ ) did not differ substantially from the reference values ( $R_{ref}$  and  $\sigma R_{ref}$ ), however, anomalies were seen in some cases. The cases where JMA data were judged as "misaligned" are as follows: both the average and standard deviation of JMA data higher than the references (e.g., from July to August 2018 at GCK in Figure 7, and June 2018 at SKT and April 2016 at AU-Gin in Supplementary Materials); the average of the JMA data lower than

the reference (e.g., April 2016 at PDF in Figure 7, and January 2016 at HPK and August 2015 at AU-Sam in Supplementary Materials); only the standard deviation of JMA data higher than the reference (e.g., December 2016 and April 2018 at GCK and from June to September 2018 at NZ-Bfm in Figure 7, and December 2018 at HBG in Supplementary Materials). In the period from March to April 2018, when dCOFF and dLOFF were large (Figure 4 (a) and (d)), the standard deviations of JMA data at some sites were larger than the references (e.g., TGF, FHK, and AU-Ync in Supplementary Materials). In some cases, the averages and standard deviations of both JMA and CEReS data were higher than the references (e.g., from July to September 2018 at IRI and many cases at AU-APL in Supplementary Materials). The cases imply misalignments of both JMA and CEReS data, or the evaluation failure due to the overlooking of cloud detection. The cases where CEReS data were judged as "misaligned" were also found (e.g., April 2018 at AU-Sam). However, as shown in the histograms on the right-hand in Figure 7 and Supplementary Materials, at all sites, the misalignment of CEReS data was less frequent.

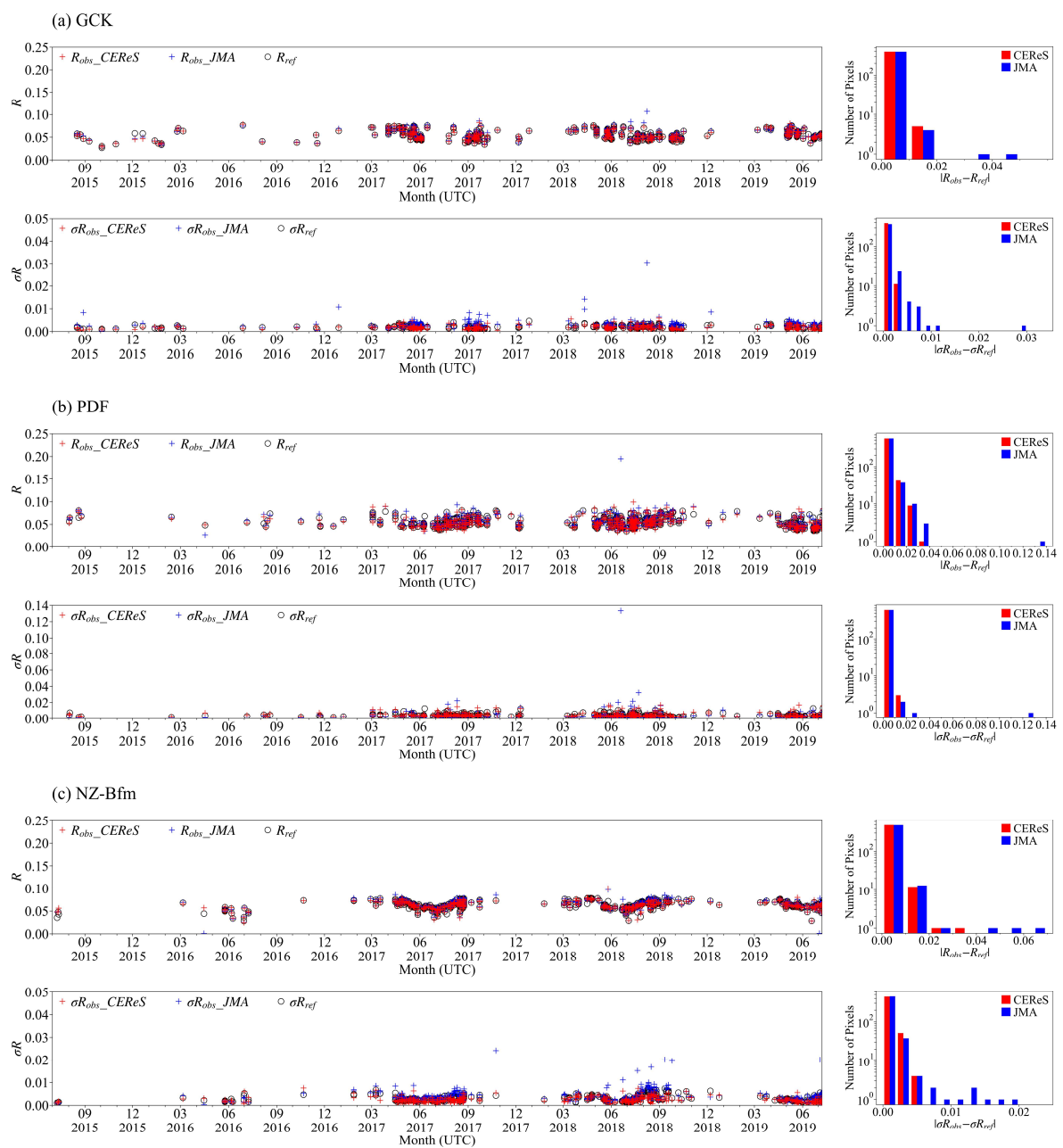


**Figure 7.** Results of the stability evaluation in (a) GCK, (b) PDF, and (c) NZ-Bfm. Upper left-hand: time series of  $R_{obs\_CEReS}$ ,  $R_{obs\_JMA}$ , and  $R_{ref}$ . Upper right-hand: histogram of  $R_{obs\_CEReS} - R_{ref}$  (red) and  $R_{obs\_JMA}$

–  $R_{ref}$  (blue). Lower left-hand: Similar to upper left-hand but for  $\sigma R_{obs\_CEReS}$ ,  $\sigma R_{obs\_JMA}$ , and  $\sigma R_{ref}$ . Lower right-hand: Similar to upper right-hand but for  $\sigma R_{obs\_CEReS} - \sigma R_{ref}$  (red) and  $\sigma R_{obs\_JMA} - \sigma R_{ref}$  (blue).

#### 4. Discussion

The relative evaluation of geolocation accuracies clarified the magnitude and direction of systematic geolocation error and periods with frequent anomalies. The information on long-term diagnostics will provide feedback with which to improve geometric corrections. The inter-comparison of different geocorrected data can calculate an objective error that differs from errors calculated from each geometric correction method itself. The results showed that geolocation errors in the JMA data were within 2 pixels in most cases. The accuracy meets quality requirements for GOES-16 and -17 [24], indicating the validity and stability of JMA infrared band data. Furthermore, a tendency for greater errors in the west–east scan direction than in the north–south direction was consistent with that of GOES-16 and -17 [24]. However, many relative errors were much greater than 1 pixel in AHI band 3 and there were error trends on various time scales. Therefore, an improvement in subpixel interpolation or geometrical correction using a visible/near-infrared band should be required for visible/near-infrared observations and studies focusing on small-scale phenomena such as urban or agricultural areas.

The shifts in the temporal trend of dCOFF/dLOFF can be caused by changes in the geolocation accuracy of JMA data. For example, the temporal shift after November–December 2016 may be due to the improvement in image navigation performance, as reported by the Meteorological Satellite Center of JMA [35]. The image navigation method may have been changed from the XC method to the POC method because the Meteorological Research Note [36] stated that the XC method was applied about the beginning of the operation of Himawari-8. JMA reported that the geolocation of JMA data had been modified to shift to east and slightly north [35]. This indicates a decrease in mean dCOFF and a slight increase in mean dLOFF, which is consistent with the shifts shown in Figure 4. Besides, the Himawari-8/AHI event logs [35] reported a decrease in image navigation accuracy, due to a spacecraft anomaly in March 2018, which is thought to have been the cause of the large dCOFFs between March and April 2018.

The diurnal change in dCOFF (Figure 5) could be due to effects of the shadow of the solar reflective band used in geometric correction by CEReS. The pattern matching in the process of CEReS data generation reflected terrain shadows that have low reflectance and shapes corresponding to terrain features. The geolocation of CEReS data shifted more westward in the morning, which is consistent with the dCOFF being lower than that in the afternoon. However, the range of the diurnal change of dCOFF was within  $\pm 1$  pixel with band 3 spatial resolution. The use of NDVI instead of band 3 reflectance may reduce the effects of shadows, because NDVI is less sensitive to shadows than reflectance and makes the boundary between land and water surfaces clear. Although the spatial resolution of band 4 (approximately 1 km) is coarser than that of band 3, it could overcome the drawbacks of both the JMA and CEReS data (coarse spatial resolution and shadow effects, respectively).

The decrease in dCOFF from March–October after 2017, shown in Figure 4 (a), could be due to increases in the frequency of low dCOFF over mid and high latitudes in the Northern and Southern Hemispheres (see Figure 6 (c) vs (d)). The high frequencies in these areas during this period may be due to high cloud cover; that is, the geolocation accuracy deteriorated due to the reduction of clear-sky pixels used for pattern matching and an increase in the effects of cloud contamination. From the spring equinox to the autumn equinox, the Northern Hemisphere is warm and wet even at mid and high latitudes, resulting in more cloud cover. On the other hand, mid and high latitudes in the Southern Hemisphere are generally geometrically corrected using the coastal areas of New Zealand and southern Australia as landmarks. In this region, the seasonal change in precipitation is not as large as that in the Northern Hemisphere, but the amount of rainfall generally does increase from the spring to the autumn equinox [37]. Furthermore, a high frequency of rainfall throughout the year near the equator would also cause a high cloud cover. These effects of clouds on geolocation are considered to be more sensitive to JMA data that use infrared bands with a low spatial resolution.

The distance in the difference of the relative geolocation of one pixel at mid and high latitudes is thus much larger than that around the sub-satellite point. Therefore, geometric correction by CEReS is considered to have a high impact, particularly at mid and high latitudes.

A number of landmark chips available could possibly enhance the diurnal and seasonal trends in relative geolocation error. From the above, the diurnal change in dCOFF may have been due to the effects of shadows in the geometric correction using the CEReS data, while the seasonal change may have been caused by the low spatial resolution of the geometric correction using the JMA data. Both effects appeared markedly in the mornings, and it is thought that a geometric correction at that time had fewer landmark chips than in the afternoon. In the morning, islands in the west Pacific are used as landmarks for geometric correction; in the afternoon, the Asian continent is included. Therefore, geolocation accuracy should be more stable in the afternoon.

The evaluation of stability captured the contamination of the high/low reflectance surface and the changes in the spatial dispersion of the  $3 \times 3$  reflectances, due to a misalignment. Geometric correction between the JMA and CEReS data has different advantages and disadvantages, due to differences in spatial resolution and wavelength characteristics. It is difficult to conclude which is better, because there is no perfect geometric correction method that can evaluate all their disadvantages. However, the stability evaluation in this study showed that the CEReS data was more stable than the JMA data for unexpected large misalignments.

## 5. Conclusions

This study determined whether JMA data or CEReS data is more suitable for terrestrial remote sensing, which requires precise geometric accuracy. To this end, we compared the COFF/LOFF difference between JMA data and CEReS data and evaluated the stabilities of JMA data and CEReS data in the fixed-site monitoring of clear-sky reflectance under the condition of dCOFF/dLOFF differences greater than 2 pixels.

The inter-comparison of geolocation between JMA data and CEReS data showed that JMA data maintained the geolocation accuracy within approximately 2 pixels over a long period of time. A change in the geolocation trend after December 2016, which could be attributed to the improvement of the image navigation performance of JMA, and occasional shifts greater than 2 pixels were also found. After the improvement of the image navigation performance, the geolocation difference from CEReS data became small. This result implies the high stability of CEReS data because CEReS has performed the same geometric correction consistently throughout the period. We believe that the long-term stability of CEReS data will be very effective in the dynamic monitoring of land surfaces using visible/near-infrared bands. However, in the comparison focusing on the diurnal cycle of the geolocation difference, a diurnal tendency was found, which may be due to shadows. Although the diurnal change was within 1 pixel, it will pose a problem in geometric correction using a visible band.

In the stability evaluation, we detected anomalies in the reflectance of JMA data during the period when large geolocation differences were observed. The cases with three consecutive scenes of  $3 \times 3$  clear-sky pixels being used in the stability evaluation are rare situations. In actual observations, more geolocation errors of JMA data are likely to occur. When targeting a small spatial scale, such as an urban or agricultural area, a fluctuation in reflectance due to a misalignment becomes a serious problem. CEReS data can provide more reliable results in such small-scale analyses.

The high stability of the geometric position of CEReS data may be effective for combined use with other sensors, such as MODIS. The combined use generally requires the averaging of values with surrounding pixels (e.g.,  $3 \times 3$  pixels) to reduce misalignment-derived noise. CEReS data may facilitate pixel-by-pixel comparison without the averaging process.

Furthermore, the geolocation accuracy of the CEReS data might be effective, not only for terrestrial monitoring, but also for atmospheric observation, and coastal water vegetation monitoring [38]. For example, atmospheric motion vectors (AMVs) [39, 40] are calculated by tracking the temporal shifts in similarly shaped clouds and water vapor. Therefore, the irregular shifts due to the misalignment of geometric corrections reduce the reliability of AMV estimations. The stability of the

CEReS data has the potential to contribute to improvements in the estimation and application (e.g., assimilation to numerical weather prediction) of AMVs.

**Supplementary Materials:** The following are available online at [www.mdpi.com/2072-4292/12/9/1372/s1](http://www.mdpi.com/2072-4292/12/9/1372/s1), Figure S1: Results of the stability evaluation in 12 sites other than the 3 sites shown in Figure 7. Upper left-hand: time series of  $R_{obs\_CEReS}$ ,  $R_{obs\_JMA}$ , and  $R_{ref}$ . Upper right-hand: histogram of  $R_{obs\_CEReS} - R_{ref}$  (red) and  $R_{obs\_JMA} - R_{ref}$  (blue). Lower left-hand: similar to the upper left-hand but for  $\sigma R_{obs\_CEReS}$ ,  $\sigma R_{obs\_JMA}$ , and  $\sigma R_{ref}$ . Lower right-hand: similar to the upper right-hand but for  $\sigma R_{obs\_CEReS} - \sigma R_{ref}$  (red) and  $\sigma R_{obs\_JMA} - \sigma R_{ref}$  (blue).

**Author Contributions:** Conceptualization, Y.Y., K.I.; methodology, Y.Y., H.T.; software, Y.Y.; validation, Y.Y.; formal analysis, Y.Y.; investigation, Y.Y.; resources, Y.Y., K.I.; writing—original draft preparation, Y.Y., K.I.; writing—review and editing, K.I., A.H.; visualization, Y.Y.; supervision, K.I.; project administration, K.I., A.H.; funding acquisition, Y.Y., A.H.

**Funding:** This study is supported by the Virtual Laboratory (VL) project, supported by the Ministry of Education, Culture, Sports, Science and Technology (MEXT), Japan, and a research grant of the Japan Society for the Promotion of Science (JSPS), KAKENHI (19K24379).

**Conflicts of Interest:** The authors declare no conflict of interest.

## References

- Bessho, K.; Date, K.; Hayashi, M.; Ikeda, A.; Imai, T.; Inoue, H.; Kumagai, Y.; Miyasaka, T.; Murata, H.; Ohno, T.; et al. An Introduction to Himawari-8/9—Japan's New-Generation Geostationary Meteorological Satellites. *J. Meteorol. Soc. Jpn. Ser. II* **2016**, *94*, 151–183.
- Jiang, Z.; Huete, R.A.; Didan, K.; Miura, T. Development of a two-band enhanced vegetation index without a blue band. *Remote Sens. Environ.* **2008**, *112*, 3833–3845.
- Miura, T.; Nagai, S.; Takeuchi, M.; Ichii, K.; Yoshioka, H. Improved Characterisation of Vegetation and Land Surface Seasonal Dynamics in Central Japan with Himawari-8 Hypertemporal Data. *Sci. Rep.* **2019**, *9*, 1–12.
- Imai, T.; Yoshida, R. *Algorithm Theoretical Basis for Himawari—8 Cloud Mask Product*; Japan Meteorological Agency: Tokyo, Japan, 2016; p. 17.
- Yamamoto, Y.; Ishikawa, H. Thermal land surface emissivity for retrieving land surface temperature from Himawari-8. *J. Meteorol. Soc. Jpn.* **2018**, *96B*, 43–58, doi:10.2151/jmsj.2018-004.
- Chen, Y.; Sun, K.; Chen, C.; Bai, T.; Park, T.; Wang, W.; Nemani, R.R.; Myneni, R.B. Generation and evaluation of LAI and FPAR products from Himawari-8 advanced Himawari imager (AHI) data. *Remote Sens.* **2019**, *11*, 1517.
- Yamamoto, Y.; Ishikawa, H.; Oku, Y.; Hu, Z. An algorithm for land surface temperature retrieval using three thermal infrared bands of Himawari-8. *J. Meteorol. Soc. Jpn.* **2018**, *96B*, 59–76.
- Damiani, A.; Irie, H.; Horio, T.; Takamura, T.; Khatri, P.; Takenaka, H.; Nagao, T.; Nakajima, T.Y.; Cordero, R.R. Evaluation of Himawari-8 surface downwelling solar radiation by ground-based measurements. *Atmos. Meas. Tech.* **2018**, *11*, 2501–2521.
- Yamamoto, Y.; Ishikawa, H. Spatiotemporal variability characteristics of clear-sky land surface temperature in urban areas of Japan observed by Himawari-8. *Sola* **2018**, *14*, 179–184.
- Yamamoto, Y.; Ishikawa, H. Influence of urban spatial configuration and sea breeze on land surface temperature on summer clear-sky days. *Urban Clim.* **2020**, *31*, 100578.
- Jang, E.; Kang, Y.; Im, J.; Lee, D.W.; Yoon, J.; Kim, S.K. Detection and monitoring of forest fires using Himawari-8 geostationary satellite data in South Korea. *Remote Sens.* **2019**, *11*, 271.
- Xiao, X.; Boles, S.; Frolking, S.; Salas, W.; Moore, B.; Li, C.; He, L.; Zhao, R. Observation of flooding and rice transplanting of paddy rice fields at the site to landscape scales in China using VEGETATION sensor data. *Int. J. Remote Sens.* **2002**, *23*, 3009–3022.
- Xiao, X.; Boles, S.; Liu, J.; Zhuang, D.; Frolking, S.; Li, C.; Salas, W.; Moore, B. Mapping paddy rice agriculture in southern China using multi-temporal MODIS images. *Remote Sens. Environ.* **2005**, *95*, 480–492.
- Shekarforoush, H.F.; Zerubia, J.B.; Member, S.; Berthod, M. Extension of Phase Correlation to Subpixel Registration. *IEEE Trans. Image Process.* **2002**, *11*, 188–200.

15. Skakun, S.; Roger, J.; Vermote, E.F.; Masek, J.G.; Justice, C.O. Automatic sub-pixel co-registration of Landsat-8 Operational Land Imager and Sentinel-2A Multi-Spectral Instrument images using phase correlation and machine learning based mapping Automatic sub-pixel co-registration of Landsat-8 Operational Land. *Int. J. Digit. Earth* **2017**, *10*, 1253–1269.
16. Meteorological Satellite Center of JMA, Himawari Navigation Monitoring Guide. Available online: <https://www.data.jma.go.jp/mscweb/data/monitoring/HimawariNaviGuide.html> (accessed on 15 March 2020).
17. Meteorological Satellite Center of JMA, Himawari-8 Image Landmark Analysis Map. Available online: [https://www.data.jma.go.jp/mscweb/data/monitoring/landmark/h8\\_landmark.html](https://www.data.jma.go.jp/mscweb/data/monitoring/landmark/h8_landmark.html) (accessed on 15 March 2020).
18. Wang, W.; Li, S.; Hashimoto, H.; Takenaka, H.; Higuchi, A.; Kalluri, S.; Nemani, R. An Introduction to the Geostationary-NASA Earth Exchange (GeoNEX) Products: 1. Top-of-Atmosphere Reflectance and Brightness Temperature. *Remote Sens.* **2020**, *12*, 1267.
19. Matsuoka, M.; Honda, R.; Nonomura, A.; Moriya, H.; Akatsuka, S.; Yoshioka, H.; Takagi, M. A Method to Improve Geometric Accuracy of Himawari-8/AHI “Japan Area” Data. *J. Jpn. Soc. Photogramm. Remote Sens.* **2015**, *54*, 280–289.
20. Vermote, F.E.; Saleous, Z.E.N.; Justice, O.C. Atmospheric correction of MODIS data in the visible to middle infrared: First results. *Remote Sens. Environ.* **2002**, *83*, 97–111.
21. Wolfe, R.E.; Nishihama, M.; Fleig, A.J.; Kuyper, J.A.; Roy, D.P.; Storey, J.C.; Patt, F.S. Achieving sub-pixel geolocation accuracy in support of MODIS land science. *Remote Sens. Environ.* **2002**, *83*, 31–49.
22. Wolfe, R.E.; Nishihama, M.; Lin, G.; Tewari, K.P.; Montano, E. MODIS and VIIRS Geometric Performance Comparison. In Proceedings of the 2012 IEEE International Geoscience and Remote Sensing Symposium; Munich, Germany, 22–27 July 2012; pp. 5017–5020.
23. Tan, B.; Dellomo, J.J.; Folley, C.N.; Grycewicz, T.J.; Houchin, S.; Isaacson, P.J.; Johnson, P.D.; Porter, B.C.; Reth, A.D.; Thiyanaratnam, P.; et al. GOES-R series image navigation and registration performance assessment tool set. *J. Appl. Remote Sens.* **2020**, *14*, 032405, doi:10.1117/1.JRS.14.032405.
24. Jeong, J.; Han, H.; Park, Y. Geometric accuracy analysis of the Geostationary Ocean Color Imager (GOCI) Level 1B (L1B) product. *Opt. Express* **2020**, *28*, 7634.
25. Wolfe, R.E.; Nishihama, M. Trends in MODIS Geolocation Error Analysis. In Proceedings of the International Society for Optical Engineering, San Diego, CA, USA, 2–4 August 2009; p. 7.
26. Xu, W.; Wooster, M.J.; Kaneko, T.; He, J.; Zhang, T.; Fisher, D. Major advances in geostationary fire radiative power (FRP) retrieval over Asia and Australia stemming from use of Himawari-8 AHI. *Remote Sens. Environ.* **2017**, *193*, 138–149.
27. Zhang, W.; Xu, H.; Zheng, F. Aerosol optical depth retrieval over East Asia using Himawari-8/AHI data. *Remote Sens.* **2018**, *10*, 137.
28. Lim, H.; Choi, M.; Kim, J.; Kasai, Y.; Chan, P.W. AHI/Himawari-8 Yonsei aerosol retrieval (YAER): Algorithm, validation and merged products. *Remote Sens.* **2018**, *10*, 699.
29. Yan, X.; Li, Z.; Luo, N.; Shi, W.; Zhao, W.; Yang, X.; Jin, J. A minimum albedo aerosol retrieval method for the new-generation geostationary meteorological satellite Himawari-8. *Atmos. Res.* **2018**, *207*, 14–27.
30. Ge, B.; Li, Z.; Liu, L.; Yang, L.; Chen, X.; Hou, W.; Zhang, Y.; Li, D.; Li, L.; Qie, L. A Dark Target Method for Himawari-8/AHI Aerosol Retrieval: Application and Validation. *IEEE Trans. Geosci. Remote Sens.* **2019**, *57*, 381–394.
31. Yan, D.; Zhang, X.; Nagai, S.; Yu, Y.; Akitsu, T.; Nasahara, K.N.; Ide, R.; Maeda, T. Evaluating land surface phenology from the Advanced Himawari Imager using observations from MODIS and the Phenological Eyes Network. *Int. J. Appl. Earth Obs. Geoinf.* **2019**, *79*, 71–83.
32. Release Note of “HIMAWARI 8” Gridded Data for Full-Disk (FD) Observation Mode. Available online: [http://www.cr.chiba-u.jp/databases/GEO/H8\\_9/FD/index.html](http://www.cr.chiba-u.jp/databases/GEO/H8_9/FD/index.html) (accessed on 15 March 2020).
33. AsiaFlux Home Page. Available online: [http://asiaflux.net/?page\\_id=22](http://asiaflux.net/?page_id=22) (accessed on 15 March 2020).
34. OzFlux Home Page. Available online: <http://www.ozflux.org.au/monitoringsites/index.html> (accessed on 15 March 2020).
35. Meteorological Satellite Center of JMA, Himawari-8 Irregular Event Logs. Available online: [https://www.data.jma.go.jp/mscweb/en/oper/event\\_H8.html](https://www.data.jma.go.jp/mscweb/en/oper/event_H8.html) (accessed on 15 March 2020).

36. Nakayama, R.; Okuyama, A. Chapter 3: Image Navigation and Calibration. In *Meteorological Research Note*; Okamoto, K., Bessho, K., Yoshizaki, Y., Murata, H., Eds.; Japan Meteorological Agency: Tokyo, Japan, 2018; Volume 238, pp. 23–37.
37. Sansom, J.; Thomson, P.; Carey-Smith, T. Stochastic seasonality of rainfall in New Zealand. *J. Geophys. Res. Atmos.* **2013**, *118*, 3944–3955.
38. Chen, X.; Shang, S.; Lee, Z.; Qi, L.; Yan, J.; Li, Y. High-frequency observation of floating algae from AHI on Himawari-8. *Remote Sens. Environ.* **2019**, *227*, 151–161.
39. Otsuka, M.; Seko, H. Characteristics of Himawari-8 Rapid Scan Atmospheric Motion Vectors Utilized in Mesoscale Data Assimilation. *J. Meteorol. Soc. Jpn.* **2018**, *96B*, 111–131.
40. Kim, D.H.; Kim, H.M. Effect of assimilating Himawari-8 atmospheric motion vectors on forecast errors over East Asia. *J. Atmos. Ocean. Technol.* **2018**, *35*, 1737–1752.



© 2020 by the authors. Licensee MDPI, Basel, Switzerland. This article is an open access article distributed under the terms and conditions of the Creative Commons Attribution (CC BY) license (<http://creativecommons.org/licenses/by/4.0/>).